

Near-field Nanoscopy of Terahertz Polaritons with Quantitative Dielectric Mapping

Xiao Guo,[†] Xin He,^{‡,¶} Zach Degnan,[‡] Bogdan C. Donose,[†] Karl Bertling,[†] Arkady Fedorov,^{‡,¶} Aleksandar D. Rakic,^{*,†} and Peter Jacobson^{*,‡}

[†]*School of Information Technology and Electrical Engineering, The University of Queensland, Brisbane, QLD 4072, Australia*

[‡]*School of Mathematics and Physics, The University of Queensland, Brisbane, QLD 4072, Australia*

[¶]*ARC Centre of Excellence for Engineered Quantum Systems, Brisbane, QLD 4072, Australia*

E-mail: a.rakic@uq.edu.au; p.jacobson@uq.edu.au

Abstract

Terahertz waves find broad use in physics, chemistry, and engineering for sensing applications. However, most experiments operate in the far-field, which precludes the observation of nanoscale features that affect the material response. Here, we use terahertz scanning near-field optical microscopy to investigate the near-field properties of coplanar waveguides fabricated from simple materials - aluminum and silicon. Using a recently developed vector calibration method in tandem with hyperspectral terahertz nano-imaging, we observe tightly confined fringes within lightly doped silicon adjacent to the silicon/aluminum interface. We attribute these fringes to a spoof surface plasmon polariton, show that the dimensions of the metal structure governs the spatial extent of the evanescent wave at the metal-semiconductor interface, and observe that removing

surface oxides enhances the THz scattering response. Our near-field observations open the pathway to aid the design of on-chip THz devices based on standard materials (silicon, aluminum) for higher efficiency photoswitches, optoelectronic detectors, and as a diagnostic tool for surface characterization.

Keywords

scattering-type scanning near-field optical microscopy (s-SNOM), THz, nanoimaging, nanospectroscopy, polaritons

1 Introduction

Surface plasmon polaritons (SPPs) are collective electromagnetic excitations that propagate at the dielectric-conductor interface. These collective excitations are formed by the coupling of incident electromagnetic waves to free electrons and are bound to material interfaces, where they exhibit maximum amplitudes and have a characteristic evanescent behavior.¹⁻³ Due to their strong confinement at interfaces, SPPs form the basis of high-precision sensors that can detect minute changes when the local dielectric properties are altered. Therefore, SPPs from visible to far-infrared wavelengths are an area of intense study for applications in sensing and telecommunications, materials characterization (including surface-enhanced Raman spectroscopy), and enhanced photovoltaic conversion efficiency for solar cells. SPPs have also been explored for optical data storage devices and plasmon-based detectors from optical to microwave frequencies.⁴⁻¹¹

Within this frequency range, terahertz (THz) frequencies are increasingly used to study condensed matter systems as this band fortuitously matches numerous energy scales in solids.¹² Therefore, THz radiation is well-suited to measure charge transport and resonantly probe plasmons or phonons among other elementary excitations and quasiparticles.¹³ However, in the THz regime, most metals can be considered perfect electrical conductors due

to their large permittivity.¹⁴ This means that THz SPPs are weakly confined to the metal surfaces^{14–16} since their plasma frequencies are far outside the THz regimes.

To confine SPPs in the THz range,^{17,18} it is necessary to tailor materials such that they have a plasma frequency within the THz band. This localized confinement for SPPs can be realized by creating sub-wavelength patterned structures including holes and corrugations on the materials. Such a surface patterning approach on conducting materials, initially realized by Pendry et al.,¹⁹ was then applied to THz radiation to enhance SPPs on patterned semiconductor substrates, including doped silicon.^{20–23} Therefore, surface patterning represents an effective method for enhancing transmission of THz waves through a sub-wavelength aperture.²⁴ A frequently encountered example is aperture-type scanning near-field optical microscopy (SNOM).^{25–27} Recently, THz SPPs have been observed^{28–30} using scattering-type SNOM (s-SNOM), excited either by the visible incident field²⁸ or directly by THz waves.^{29,30} As a nanoscopy, THz s-SNOM is able to unravel THz features at the nanoscale.^{31–35} It aids understanding of the detection and generation mechanism of THz nanophotonic devices.^{36,37} Terahertz s-SNOM has been employed to characterize surface-confined electromagnetic responses in micro-structures,^{38–40} study carriers plasmon^{41,42} and phonon polaritons⁴³ in van der Waals materials, track Dirac fermion density transitions,²⁹ and reveal Dirac plasmon polaritons in topological materials³⁰ at sub-micron resolution. These demonstrate the potential of resolving evanescent behaviors at the nanoscale.

In this work, we show that a conceptually simple coplanar waveguide structure fabricated from aluminum and silicon supports spoof SPPs. We detect the existence, and investigate the characteristics of spoof SPPs supported within this structure by using THz s-SNOM.⁴⁴ By combining THz time-domain spectroscopy with the high spatial resolution of the s-SNOM we are able to resolve nanoscale features and broadband THz spectral response of the SPPs. We find that the spatial variation of the permittivity matches well the oscillatory behavior of the SPP's edge fringes. By effectively altering the dielectric environment, corrugated surfaces supporting spoof plasmons can potentially enhance nano-scale light-matter interactions. It

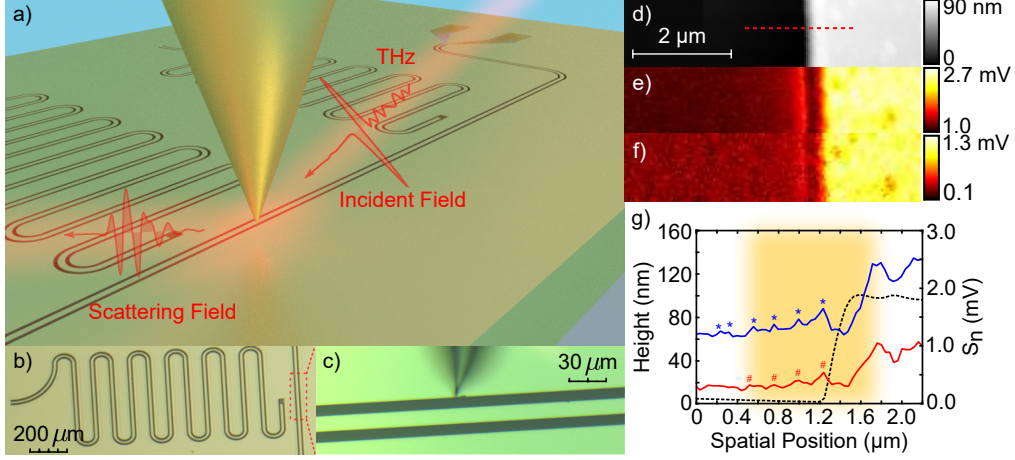


Figure 1: (a) Schematic of THz s-SNOM experiments on a chip with coplanar microwave resonators, (b) optical micrograph of an individual coplanar microwave resonator, (c) the area of interest under THz s-SNOM, a scanning area across deposited Al film and etched Si channel: (d) topography, THz near-field scattering signals demodulated at the first-order (e) and second-order (f) harmonics of the tapping frequency, and (g) the height profile (black) and corresponding THz white-light scattering amplitudes (blue for (e), red for (f)) obtained from the line scan denoted by the red broken line in (d). Oscillation peaks are highlighted by markers (\star for S_1 , $\#$ for S_2). The orange shaded area in (g) was selected to perform THz hyperspectral imaging.

opens the door for future nanoplasmonic applications, including molecular identification, biochemical sensors, and other optoelectronic on-chip applications in the THz or lower frequency regimes of the electromagnetic spectrum.^{45–49}

2 Results

Figure 1a shows a 3D rendering of the chip under investigation combined with a schematic representation of the scattering SNOM geometry. As fabricated devices are $\lambda/4$ coplanar microwave resonators with dimensions chosen to ensure 50Ω impedance matching; $8 \mu\text{m}$ wide wet etched gaps bounding the $14 \mu\text{m}$ transmission line [Fig. 1 (b) & (c)].⁵⁰ The region of interest for our s-SNOM investigations is the etched domain defining the transmission line. The same microscopic region was repeatedly investigated with multiple tips and in different device orientations by using a small notch defect in the aluminum film as a position marker [Fig. 1 (c)]. Tapping mode AFM imaging in Fig. 1 (d) reveals that the device is

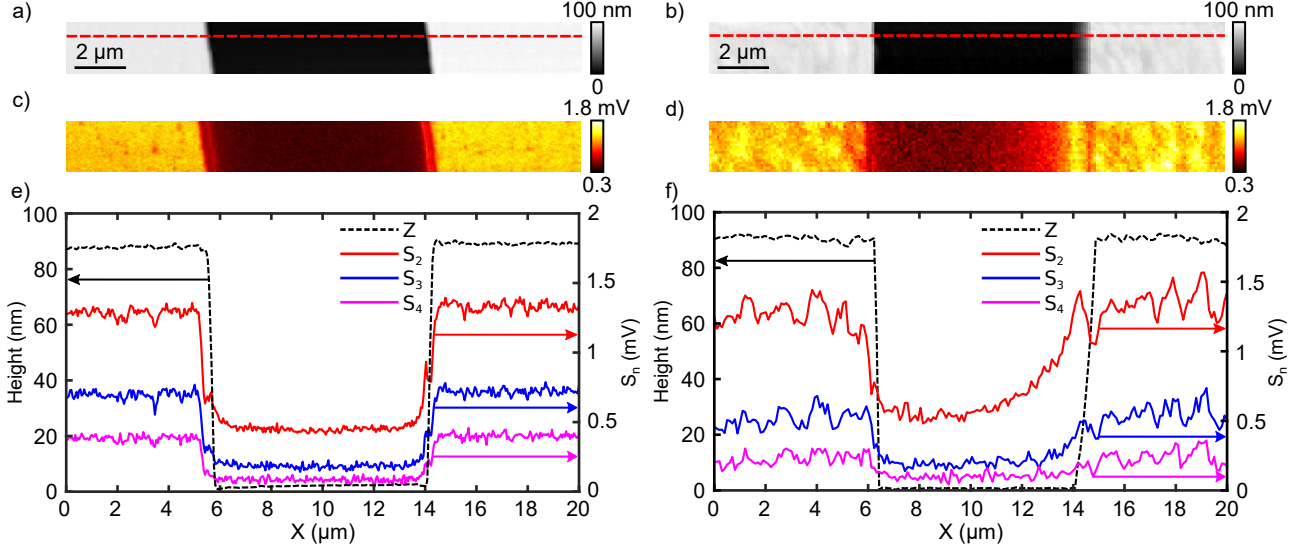


Figure 2: Comparison of topography (a), (b) and THz near-field scattering amplitudes (c), (d) between the as-prepared and 2-sec BOE etch chip respectively under the same probe tapping amplitude. Spatial variation of different harmonics of THz white-light near-field scattering amplitudes (solid lines, S_2 : red, S_3 : blue, S_4 : magenta) and the concurrently measured topography (black, the broken line) across Al-Si-Al interface are shown in (e) and (f) respectively.

dominated by a sharp 85 nm step demarcating the aluminum and silicon regions. Turning to the THz scattering signals, we observe a prominent increase in scattered intensity just within the silicon channel for both the first (S_1) and second-harmonics (S_2) of the signal [Fig. 1 (e) & (f)]. By extracting a sequence of line profiles across the boundary, we observe a series of oscillations within the S_1 and S_2 signals. Given the abrupt change in permittivity (positive to negative) at the semiconductor-metal interface, we attribute these features on the microstructured device to spoof SPP caused by the incident THz stimulus.

To rule out purely local effects in the THz scattering behavior, we performed measurements across the whole width of the etched channel (Fig. 2). Second-harmonic (S_2) imaging across the 8 μm wide channel reveals bands of increased scattering in proximity to both aluminum contacts [Fig. 2 (c) & (d)]. The scattered THz signal decays with distance from the aluminum-silicon boundary while the scattered signal parallel to the boundary remains constant. To better quantify the decay characteristics of the scattered THz amplitude, line profiles were acquired at higher harmonics (S_2 , S_3 , S_4) of the cantilever oscillation frequency

to rule out spurious background signals [Fig. 2 (c)]. For all harmonics, the enhanced scattering extends substantially into the silicon channel, nearly 1 μm for the S_2 signal, which is substantially larger than the estimated spatial resolution of 130 nm (see supplementary materials, Fig. S1). Collectively, these line profiles show consistent exponential decay of the scattered THz amplitude within the silicon channel. From the line profiles in Fig. 2 (e), we observe that the reflectivity of the aluminium film of the microwave feedline is weaker than the reflectivity of the ground. This difference in the THz amplitude of the scattering signal (and the reflectivity) between the ground and the floating microwave feedline, essentially a difference between the reflectivity of grounded and the floating features, has been observed and explained earlier by Chen and co-workers.⁵¹

By defining the scattering asymmetry ratio (SAR) as $(L-R)/(L+R)$, we observe a SAR of 13% for both second and third harmonic signals in Fig. 2 (e) with the SAR increasing to 31% (S_2) and 23% (S_3) in Fig. 2 (f). We didn't use the the fourth harmonic scattering signal (S_4) due to its reduced signal-to-noise ratio. We note that the silicon region of interest is bound by aluminum films with unequal lateral extensions [Fig. 1 (a) & (b)]. The aluminum film on the left third of Fig. 2 (a) is part of the 14 μm wide microwave feedline, while the right third corresponds to the ground plane which extends upwards of $6 \times 5 \text{ mm}^2$.

As the coplanar waveguide structure was examined in ambient conditions, the exposed silicon is capped by a thin SiO_x layer. To rule out surface phonon polaritons as the origin of THz response, the sample was post-processed by a 2-second buffered oxide etch (BOE) step which selectively and rapidly removes SiO_x . Immediately after the BOE dip, the silicon channel hosts a dramatically enhanced near-field response, comparable to the aluminum film. While wet etching does not attack silicon, we observe an increase in aluminum film roughness after treatment and this is reflected in the less homogeneous scattering signal on the aluminum film. Turning to the line profiles across the BOE processed device, all higher harmonics show an increase in scattered THz amplitude with the exponentially decaying tail now extending several micrometers towards the center of the etched channel. This processing

step rules out SiO_x as the origin of the enhanced THz response within the channel.

To better understand the strong THz scattering signal adjacent to the aluminum-silicon interface, we performed hyperspectral measurements across the interface. For all panels in Fig. 3, the interface is located at a spatial position of 0 nm [Fig. 3 (a), broken line] and the examined range coincides with the orange shaded region in Fig. 2 (g). For the hyperspectral line profiles, a 10 ps THz scattering field was collected for each spatial position (step size = 40 nm) by sweeping the optical scanning delay line. The obtained hyperspectral data, taken before the BOE dip, allow us to track the spatial dependence of the localized states over the available frequency range. To avoid background signals, the second harmonic, S_2 , of the scattering signal was used to obtain the monochromatic frequency response.

In Fig. 3 (a), we plot the non-zero near-field response between 0.55 and 1.6 THz, the incident THz field contains frequency components ranging from 0 to 6 THz. The cut-off above 1.6 THz, and the varying spectral enhancement below this value, is understood to originate from the antenna resonance effect in s-SNOM, depending on the tip geometry and the dipolar resonance between the tip and sample.⁵²⁻⁵⁵ Additionally, a sharp dip in the near-field response near 1.15 THz is due to a strong water-vapor line from operating in the ambient.⁵⁶ Regarding the spatial dependence of near-field response, we observed an exponentially decaying near-field scattering amplitude on the silicon channel side adjacent to the aluminum ground plane. Figure 3 (b) shows the value of the wrapped phase jumps between $-\pi$ and π and is due to the far-field propagation phase delay. As the tip approaches the aluminum-silicon boundary (defined as 0 nm in Fig. 3), the frequency-resolved phase (ϕ) in panel b rapidly varies, we attribute this variation to edge fringes across topographical boundaries and the effective radius of the SNOM tip as discussed by Babicheva et al.⁵⁷

To better correlate the measured scattering spectrum with more intuitive metrics, such as the complex reflectivity, the system response must first be calibrated, for example by performing the baseline subtraction. Normalizing the hyperspectral line profile with a reference signal measured with the same tip on Au, we expect this quantity to be proportional to

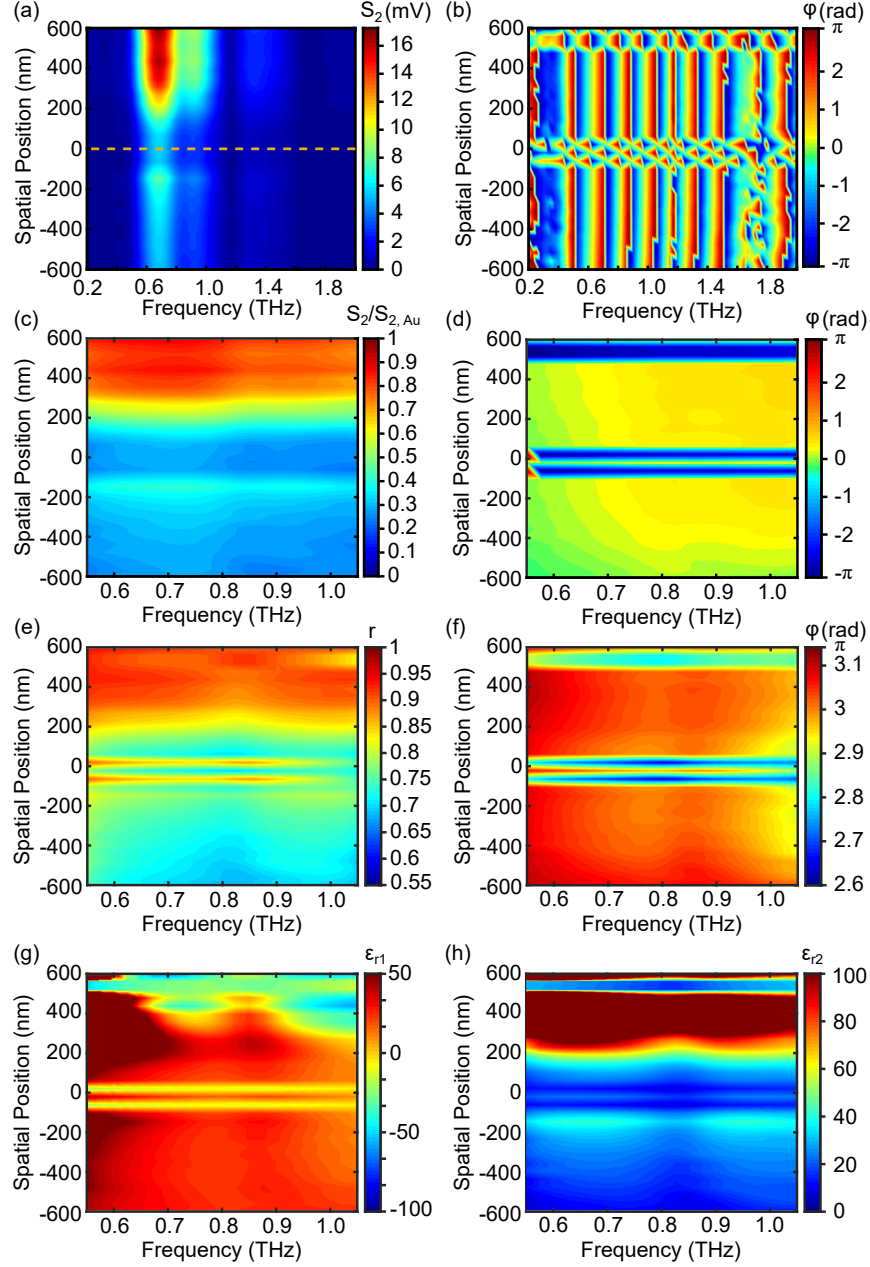


Figure 3: THz near-field hyperspectral imaging: part of the same area indicated by the red broken line in Figure 1d was selected for the hyperspectral imaging. The tip moved from the spatial position -600 nm (Si channel) to 600 nm (Al film) with the step size 40 nm, as shown by the shaded orange area in Fig. 1 (g). Hyperspectral imaging amplitude (a) and phase (b) of the second-order harmonic (S_2) of near-field scattering THz field within 0.2 to 2 THz. The same hyper-spectra (ranging from 0.55 to 1.05 THz) were calibrated by removing the baseline signal — (c) amplitude, (d) phase — obtained from a gold standard reference ($S_2/S_{2,Au}$) and by using a recently developed vector-nature method⁴⁴ — (e) amplitude, (f) phase. The corresponding spatial-varying effective dielectric permittivity — (g) real part, (h) imaginary part — were plotted using vector-nature calibration method.

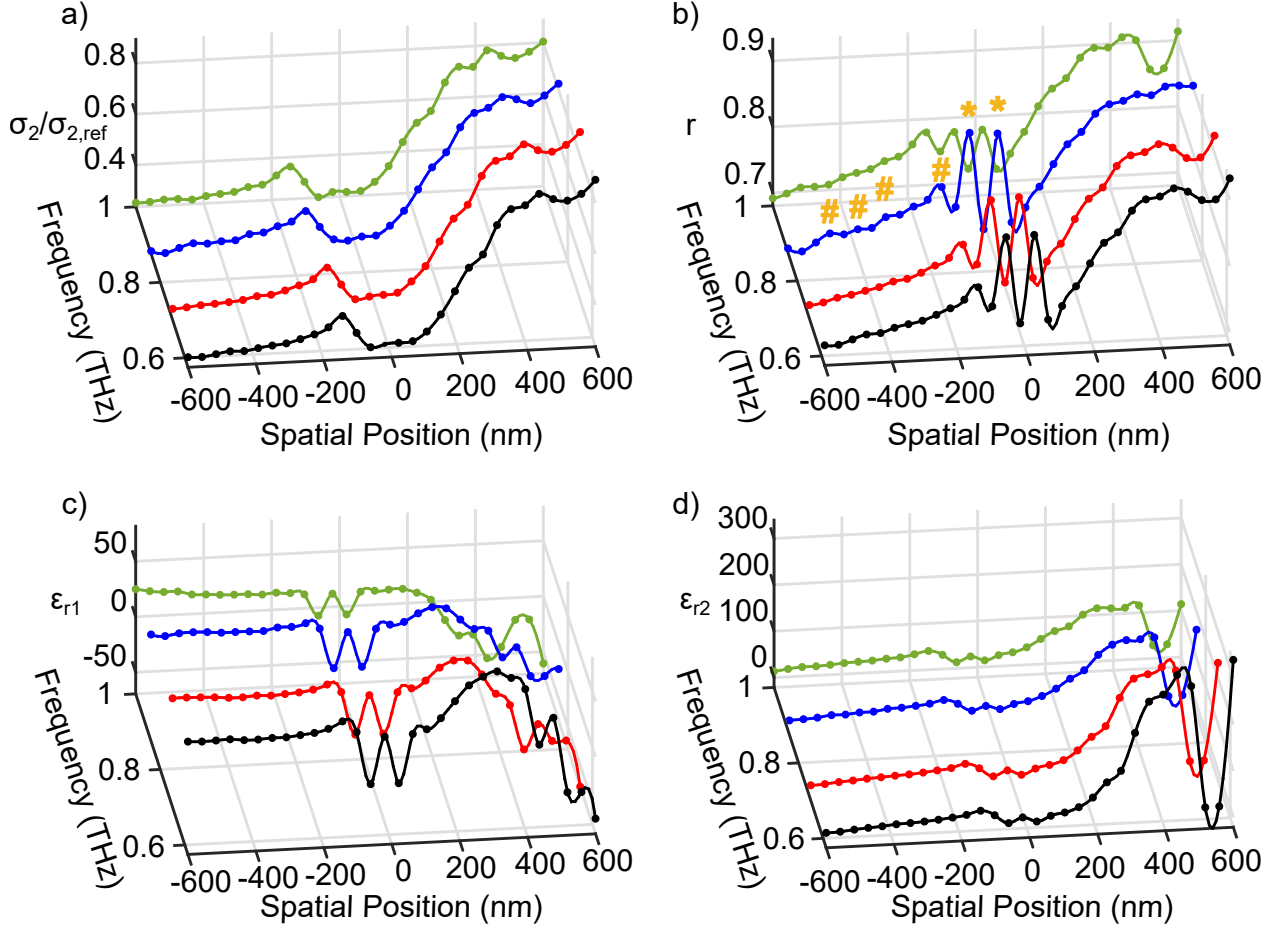


Figure 4: Spatial-varying correlation between scattering amplitude and dielectric responses at 0.575 (black), 0.7 (red), 0.85 (blue) and 1 THz (green). Scattering amplitudes were plotted for baseline-removing (a) and vector-nature (b) calibration methods. At 0.85 THz, the most representative fringe peaks same as in Fig. 1 (g) were indicated with number signs (#), and two additional peaks from the vector-nature calibration method were labeled by an asterisk (*). Permittivity (c: real and d: imaginary) at selected THz frequencies in Fig. 3 (g) & (h) were plotted, and sign flips of ϵ_{r1} were observed along the spatial position from -600 to 600 nm across Si-Al interface.

the scattered probe-sample dipole moment.^{58,59} The amplitude and phase of the normalized scattering signal are plotted in Fig. 3 (c) & (d). In Fig. 3 (c), there is a downward trend in the amplitude coinciding with the movement of the tip from aluminum to silicon. This can easily be rationalized as a transition from a high to a low scattering medium. Similarly, a local minimum is present in the middle of Fig. 3 (c), which corresponds to the start of the etched silicon channel matching the observation made in Fig. 3 (a). More intriguingly, unexpected phase jumps appear in the normalized phase [Fig. 3 (d)] on the aluminum ground

plane, around 500 nm, and at the aluminum-silicon interface (-100 to 100 nm). This indicates that an additional phase delay is incurred during the probe scanning in addition to the typical scattering phase. While this normalization procedure highlights the near-field amplitude and phase response, it does not capture the full complex nature of the amplitude scattering signal.

To reconstruct the reflectivity from the scattering amplitude, we perform a calibration using a vector method as described by Guo et al.⁴⁴ The s-SNOM system response is calibrated using reference signals from a gold mirror, high-resistivity Si, and air. These three standards allow us to extract the spatially dependent THz reflectivity [see Fig. 3 (e) & (f)]. Following calibration, two peaks appear near the aluminum-silicon interface in Fig. 3 (e). These peaks are not immediately visible when the baseline is simply subtracted, as illustrated in Fig. 3 (c).

To correlate the calibrated spatial-varying scattering behavior with dielectric responses, the extracted effective complex permittivities are plotted on Fig. 3 (g) & (h). Apart from the same peaks observed in Fig. 3 (e), Fig. 3 (g) shows the real part of permittivity ϵ_{r1} changes the sign from -600 to 600 nm spatial positions. This sign change denotes the beginning of metallic response from Al film and is supported by the large value of ϵ_{r2} shown in Fig. 3 (h). These observations of surface dielectric responses justify the dielectric condition to support surface plasmon polariton.¹⁴ To illustrate the frequency dependence of the spatially varying near-field responses we plot the amplitudes of two quantities obtained in the calibration process. Figure 4a, b plot the baseline subtraction scattering coefficient and the vector-nature calibrated reflectivity at selected THz frequencies respectively. These plots show that scattering amplitude contains an exponential decay extending away from the aluminum ground plane and into the silicon channel. The corresponding effective complex dielectric responses are shown in Fig. 4 (c) & (d). In the calibrated reflectivity, weak fringes are superimposed on the exponential decay and the imaginary part of permittivity spatially tracks the localized fringe peaks as shown in Fig. 5. Further details can be found in supplementary materials (Fig. S3 and Fig. S4).

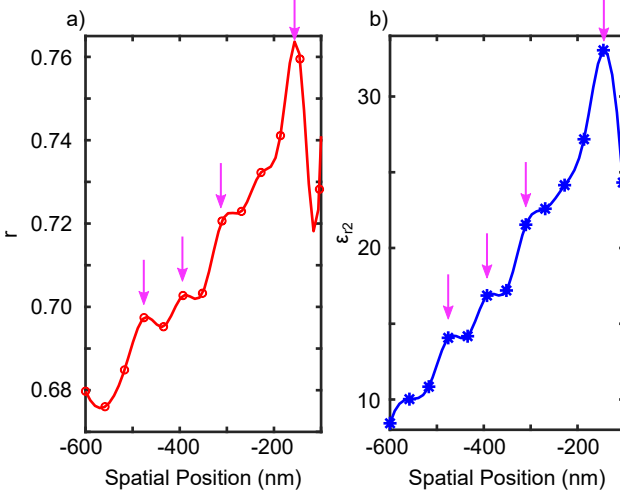


Figure 5: Spatial-varying correlation between calibrated reflectivity (r) and the imaginary part of permittivity (ϵ_{r2}) at 0.85 THz: the weak fringes superimposed on the exponential decay are highlighted with arrows.

3 Discussion

Taken together, the results presented here show the power of near-field measurements coupled with the vector calibration method to resolve nanoscale THz scattering features. This is most clearly seen in Fig. 2 (e) & (h) where our method recovers THz fringes not observed using a simple baseline subtraction. As the localized fringes are observed after a full calibration of the scattered amplitude, we conclusively rule out artifacts due to tip geometry such as multiple apices and shadow effects.⁶⁰ This case is further bolstered by considering the left-right asymmetry within the etched channel. This phenomenon can be explained by the microwave transmission line being floating.⁵¹ As this asymmetry is observed with multiple tips and in different orientations (see supplementary materials, Fig. S2), it cannot be caused by the microscopic tip structure. Since the states within the channel are localized and exponentially decay away from the aluminum film, we attribute these signatures to a spoof SPP.

Spoof SPP, as originally envisioned by Pendry, Martin-Moreno, and Garcia-Vidal,¹⁹ are found in materials patterned with features much smaller than the wavelength of the incident light. The small scale features of the microwave transmission line and etched gaps (14 μm

and 8 μm , respectively) coupled with the permittivities of opposite sign — aluminium (negative) and silicon (positive) — at terahertz frequencies, constitutes an effective medium that supports the behavior of SPPs. The observation of a spoof SPP in our sample is initially surprising given the use of a highly resistive ($> 10 \text{ k}\Omega \cdot \text{cm}$) silicon substrate. However, as determined earlier, the silicon substrate contains excess charge carriers of the order of 10^{16} cm^{-3} after wet etching of the aluminium film.⁵⁰ Furthermore, as SiO_x suppresses the near-field response and its removal enhances the response, the exponential decay behavior and fringes in our case are due to bulk carriers, and not phonon polaritons. Finally, we note that the local minimum observed on the aluminum ground plane is similar to a previously reported behavior ascribed to surface phonon polaritons in mid-infrared s-SNOM.⁵⁷ However, in our case, the polariton originates from the geometric confinement of the incident THz light.

4 Conclusions

In conclusion, using near-field THz nanoscopy on a micropatterned surface we have observed and characterized spoof surface plasmon polaritons. Using vector calibration methods, we show that proper calibration aids the enhanced identification of these signals. We note that the micropatterned device was fabricated on a standard material platform, aluminum on silicon. The simplicity of these materials, and the observed effect of a strong ground plane, will aid the development and design of more complex on-chip THz devices using silicon.

Acknowledgement

The authors acknowledge the Traditional Owners and their custodianship of the lands on which UQ operates. We pay our respects to their Ancestors and their descendants, who continue cultural and spiritual connections to Country. Financial support was provided by the Australian Research Council (DP210103342) and the ARC Centre of Excellence for En-

gineered Quantum Systems (EQUS, CE170100009). The authors acknowledge the facilities, and the scientific and technical assistance, of the Microscopy Australia Facility at the Centre for Microscopy and Microanalysis, The University of Queensland. This work was performed in part at the Queensland node of the Australian National Fabrication Facility. A company established under the National Collaborative Research Infrastructure Strategy to provide nano and microfabrication facilities for Australia's researchers.

Supporting Information Available

The following files are available free of charge.

- Sup. Mat. Near-field Nanoscopy of THz Polaritons.pdf: Supplementary figures — S1 probe tip characterization, S2 THz near-field images before and after etching with different orientations, S3 and S4: the spatial-varying relationship between reflectivity and permittivity at selected THz frequencies.

References

- (1) Ritchie, R. H. Plasma losses by fast electrons in thin films. *Phys. Rev.* **1957**, *106*, 874.
- (2) Barnes, W. L.; Dereux, A.; Ebbesen, T. W. Surface plasmon subwavelength optics. *Nature* **2003**, *424*, 824–830.
- (3) Zhang, Z.; Nest, L.; Wang, S.; Wang, S.-Y.; Ma, R.-M. Lasing-enhanced surface plasmon resonance spectroscopy and sensing. *Photonics Res.* **2021**, *9*, 1699–1714.
- (4) Fei, Z.; Rodin, A.; Andreev, G. O.; Bao, W.; McLeod, A.; Wagner, M.; Zhang, L.; Zhao, Z.; Thiemens, M.; Dominguez, G., et al. Gate-tuning of graphene plasmons revealed by infrared nano-imaging. *Nature* **2012**, *487*, 82–85.

(5) Liu, S.; Zhang, P.; Liu, W.; Gong, S.; Zhong, R.; Zhang, Y.; Hu, M. Surface polariton Cherenkov light radiation source. *Phys. Rev. Lett.* **2012**, *109*, 153902.

(6) Liu, S.; Zhang, C.; Hu, M.; Chen, X.; Zhang, P.; Gong, S.; Zhao, T.; Zhong, R. Coherent and tunable terahertz radiation from graphene surface plasmon polaritons excited by an electron beam. *Appl. Phys. Lett.* **2014**, *104*, 201104.

(7) Fei, Z.; Goldflam, M.; Wu, J.-S.; Dai, S.; Wagner, M.; McLeod, A.; Liu, M.; Post, K.; Zhu, S.; Janssen, G.; Fogler, M.; Basov, D. Edge and surface plasmons in graphene nanoribbons. *Nano Lett.* **2015**, *15*, 8271–8276.

(8) Xu, Y.; Zhang, X.; Tian, Z.; Gu, J.; Ouyang, C.; Li, Y.; Han, J.; Zhang, W. Mapping the near-field propagation of surface plasmons on terahertz metasurfaces. *Appl. Phys. Lett.* **2015**, *107*, 021105.

(9) Mitrofanov, O.; Todorov, Y.; Gacemi, D.; Mottaghizadeh, A.; Sirtori, C.; Brener, I.; Reno, J. Near-field spectroscopy and tuning of sub-surface modes in plasmonic terahertz resonators. *Opt. Express* **2018**, *26*, 7437–7450.

(10) Tang, W. X.; Zhang, H. C.; Ma, H. F.; Jiang, W. X.; Cui, T. J. Concept, theory, design, and applications of spoof surface plasmon polaritons at microwave frequencies. *Adv. Opt. Mater.* **2019**, *7*, 1800421.

(11) Yao, Z.; Xu, S.; Hu, D.; Chen, X.; Dai, Q.; Liu, M. Nanoimaging and nanospectroscopy of polaritons with time resolved s-SNOM. *Adv. Opt. Mater.* **2020**, *8*, 1901042.

(12) Spies, J. A.; Neu, J.; Tayyah, U. T.; Capobianco, M. D.; Pattengale, B.; Ostresh, S.; Schmuttenmaer, C. A. Terahertz spectroscopy of emerging materials. *J. Phys. Chem. C* **2020**, *124*, 22335–22346.

(13) Sun, Z.; Fogler, M.; Basov, D.; Millis, A. J. Collective modes and terahertz near-field response of superconductors. *Phys. Rev. Research* **2020**, *2*, 023413.

(14) Zhang, X.; Xu, Q.; Xia, L.; Li, Y.; Gu, J.; Tian, Z.; Ouyang, C.; Han, J.; Zhang, W. Terahertz surface plasmonic waves: a review. *Adv. Photon.* **2020**, *2*, 014001.

(15) Jeon, T.-I.; Zhang, J.; Grischkowsky, D. THz Sommerfeld wave propagation on a single metal wire. *Appl. Phys. Lett.* **2005**, *86*, 161904.

(16) Jeon, T.-I.; Grischkowsky, D. THz Zenneck surface wave (THz surface plasmon) propagation on a metal sheet. *Appl. Phys. Lett.* **2006**, *88*, 061113.

(17) Davoyan, A. R.; Popov, V. V.; Nikitov, S. A. Tailoring terahertz near-field enhancement via two-dimensional plasmons. *Phys. Rev. Lett.* **2012**, *108*, 127401.

(18) Chochol, J.; Postava, K.; Čada, M.; Vanwolleghem, M.; Mičica, M.; Halagačka, L.; Lampin, J.-F.; Pištora, J. Plasmonic behavior of III-V semiconductors in far-infrared and terahertz range. *J. Eur. Opt. Soc. Rapid Publ.* **2017**, *13*, 1–8.

(19) Pendry, J.; Martin-Moreno, L.; Garcia-Vidal, F. Mimicking surface plasmons with structured surfaces. *Science* **2004**, *305*, 847–848.

(20) Allen Jr, S.; Tsui, D.; Logan, R. Observation of the two-dimensional plasmon in silicon inversion layers. *Phys. Rev. Lett.* **1977**, *38*, 980.

(21) Rivas, J. G.; Kuttge, M.; Bolivar, P. H.; Kurz, H.; Sánchez-Gil, J. Propagation of surface plasmon polaritons on semiconductor gratings. *Phys. Rev. Lett.* **2004**, *93*, 256804.

(22) Hanham, S.; Fernández-Domínguez, A.; Teng, J. H.; Ang, S.; Lim, K.; Yoon, S. F.; Ngo, C.; Klein, N.; Pendry, J.; Maier, S. A. Broadband terahertz plasmonic response of touching InSb disks. *Adv. Mater.* **2012**, *24*, OP226–OP230.

(23) Li, S.; Jadidi, M. M.; Murphy, T. E.; Kumar, G. Terahertz surface plasmon polaritons on a semiconductor surface structured with periodic V-grooves. *Opt. Express* **2013**, *21*, 7041–7049.

(24) Rivas, J. G.; Schotsch, C.; Bolivar, P. H.; Kurz, H. Enhanced transmission of THz radiation through subwavelength holes. *Phys. Rev. B* **2003**, *68*, 201306.

(25) Mitrofanov, O.; Brener, I.; Wanke, M.; Ruel, R.; Wynn, J.; Bruce, A.; Federici, J. Near-field microscope probe for far infrared time domain measurements. *Appl. Phys. Lett.* **2000**, *77*, 591–593.

(26) Navarro-Cia, M.; Natrella, M.; Dominec, F.; Delagnes, J.-C.; Kužel, P.; Mounaix, P.; Graham, C.; Renaud, C.; Seeds, A.; Mitrofanov, O. Terahertz imaging of subwavelength particles with Zenneck surface waves. *Appl. Phys. Lett.* **2013**, *103*, 221103.

(27) Hale, L. L.; Keller, J.; Siday, T.; Hermans, R. I.; Haase, J.; Reno, J. L.; Brener, I.; Scalari, G.; Faist, J.; Mitrofanov, O. Noninvasive Near-Field Spectroscopy of Single Subwavelength Complementary Resonators. *Laser Photonics Rev.* **2020**, *14*, 1900254.

(28) Wiecha, M. M.; Al-Daffaie, S.; Bogdanov, A.; Thomson, M. D.; Yilmazoglu, O.; Küppers, F.; Soltani, A.; Roskos, H. G. Direct near-field observation of surface plasmon polaritons on silver nanowires. *ACS Omega* **2019**, *4*, 21962–21966.

(29) Kim, R. H. et al. Terahertz Nano-Imaging of Electronic Strip Heterogeneity in a Dirac Semimetal. *ACS Photonics* **2021**,

(30) Chen, S.; Bylinkin, A.; Wang, Z.; Schnell, M.; Chandan, G.; Li, P.; Nikitin, A. Y.; Law, S.; Hillenbrand, R. Real-space nanoimaging of THz polaritons in the topological insulator Bi_2Se_3 . *arXiv preprint arXiv:2107.10791* **2021**,

(31) Von Ribbeck, H.-G.; Brehm, M.; Van der Weide, D.; Winnerl, S.; Drachenko, O.; Helm, M.; Keilmann, F. Spectroscopic THz near-field microscope. *Opt. Express* **2008**, *16*, 3430–3438.

(32) Kuschewski, F.; von Ribbeck, H.-G.; Döring, J.; Winnerl, S.; Eng, L.; Kehr, S. Narrow-

band near-field nanoscopy in the spectral range from 1.3 to 8.5 THz. *Appl. Phys. Lett.* **2016**, *108*, 113102.

(33) Chen, X.; Hu, D.; Mescall, R.; You, G.; Basov, D.; Dai, Q.; Liu, M. Modern scattering-type scanning near-field optical microscopy for advanced material research. *Adv. Mater.* **2019**, *31*, 1804774.

(34) Rakić, A.; Taimre, T.; Bertling, K.; Lim, Y.; Dean, P.; Valavanis, A.; Indjin, D. Sensing and imaging using laser feedback interferometry with quantum cascade lasers. *Appl. Phys. Rev.* **2019**, *6*, 021320.

(35) Pogna, E. A.; Silvestri, C.; Columbo, L. L.; Brambilla, M.; Scamarcio, G.; Vitiello, M. S. Terahertz near-field nanoscopy based on detectorless laser feedback interferometry under different feedback regimes. *APL Photonics* **2021**, *6*, 061302.

(36) Alonso-González, P. et al. Acoustic terahertz graphene plasmons revealed by photocurrent nanoscopy. *Nat. Nanotechnology* **2017**, *12*, 31–35.

(37) Pogna, E. A.; Asgari, M.; Zannier, V.; Sorba, L.; Viti, L.; Vitiello, M. S. Unveiling the detection dynamics of semiconductor nanowire photodetectors by terahertz near-field nanoscopy. *Light Sci. Appl.* **2020**, *9*, 1–12.

(38) Pizzuto, A.; Chen, X.; Hu, H.; Dai, Q.; Liu, M.; Mittleman, D. M. Anomalous contrast in broadband THz near-field imaging of gold microstructures. *Opt. Express* **2021**, *29*, 15190–15198.

(39) Sulollari, N.; Keeley, J.; Park, S.; Rubino, P.; Burnett, A. D.; Li, L.; Rosamond, M. C.; Linfield, E. H.; Davies, A. G.; Cunningham, J. E.; Dean, P. Coherent terahertz microscopy of modal field distributions in micro-resonators. *APL Photonics* **2021**, *6*, 066104.

(40) Zhang, Z.; Hu, M.; Zhang, X.; Wang, Y.; Zhang, T.; Zhao, T.; Wu, Z.; Zhong, R.; Liu, D.; Wei, Y.; Gong, Y.; Liu, S. Direct observation of tip-gap interactions in THz scattering-type scanning near-field optical microscopy. *Appl. Phys. Express* **2021**,

(41) Zhang, J.; Chen, X.; Mills, S.; Ciavatti, T.; Yao, Z.; Mescall, R.; Hu, H.; Semenenko, V.; Fei, Z.; Li, H.; Perebeinos, V.; Tao, H.; Dai, Q.; Du, X.; Liu, M. Terahertz nanoimaging of graphene. *ACS Photonics* **2018**, *5*, 2645–2651.

(42) Jing, R.; Shao, Y.; Fei, Z.; Lo, C. F. B.; Ruta, F.; Staunton, J.; McLeod, A.; Sun, Z.; Chen, X.; Fogler, M.; Millis, A. J.; Liu, M.; Cobden, D. H.; Xu, X.; Basov, D. N. Terahertz response of monolayer and few-layer WTe₂ at the nanoscale. *Nat. Commun.* **2021**, *12*, 5594.

(43) de Oliveira, T. V.; Nörenberg, T.; Álvarez-Pérez, G.; Wehmeier, L.; Taboada-Gutiérrez, J.; Obst, M.; Hempel, F.; Lee, E. J.; Klopff, J. M.; Errea, I.; Nikitin, A. Y.; Kehr, S. C.; Alonso-González, P.; Eng, L. M. Nanoscale-Confined Terahertz Polaritons in a van der Waals Crystal. *Adv. Mater.* **2021**, *33*, 2005777.

(44) Guo, X.; Bertling, K.; Rakić, A. D. Optical constants from scattering-type scanning near-field optical microscope. *Appl. Phys. Lett.* **2021**, *118*, 041103.

(45) Moon, K.; Do, Y.; Park, H.; Kim, J.; Kang, H.; Lee, G.; Lim, J.-H.; Kim, J.-W.; Han, H. Computed terahertz near-field mapping of molecular resonances of lactose stereo-isomer impurities with sub-attomole sensitivity. *Sci. Rep.* **2019**, *9*, 1–8.

(46) Luan, Y.; McDermott, L.; Hu, F.; Fei, Z. Tip-and plasmon-enhanced infrared nanoscopy for ultrasensitive molecular characterizations. *Phys. Rev. Applied* **2020**, *13*, 034020.

(47) Datz, D.; Németh, G.; Walker, K. E.; Rance, G. A.; Pekker, Á.; Khlobystov, A. N.; Kamarás, K. Polaritonic Enhancement of Near-Field Scattering of Small Molecules Encapsulated in Boron Nitride Nanotubes: Chemical Reactions in Confined Spaces. *ACS Appl. Nano Mater.* **2021**, *4*, 4335–4339.

(48) Fali, A.; White, S. T.; Folland, T. G.; He, M.; Aghamiri, N. A.; Liu, S.; Edgar, J. H.; Caldwell, J. D.; Haglund, R. F.; Abate, Y. Refractive index-based control of hyperbolic phonon-polariton propagation. *Nano Lett.* **2019**, *19*, 7725–7734.

(49) Soltani, A.; Kuschewski, F.; Bonmann, M.; Generalov, A.; Vorobiev, A.; Ludwig, F.; Wiecha, M. M.; Čibiraitė, D.; Walla, F.; Winnerl, S.; Kehr, S. C.; Eng, L. M.; Stake, J.; Roskos, H. G. Direct nanoscopic observation of plasma waves in the channel of a graphene field-effect transistor. *Light Sci. Appl.* **2020**, *9*, 1–7.

(50) Guo, X.; He, X.; Degnan, Z.; Donose, B. C.; Bertling, K.; Fedorov, A.; Rakić, A. D.; Jacobson, P. Near-field terahertz nanoscopy of coplanar microwave resonators. *Appl. Phys. Lett.* **2021**, *119*, 091101.

(51) Chen, X. et al. THz near-field imaging of extreme subwavelength metal structures. *ACS Photonics* **2020**, *7*, 687–694.

(52) Wang, K.; Mittleman, D. M.; van der Valk, N. C.; Planken, P. C. Antenna effects in terahertz apertureless near-field optical microscopy. *Appl. Phys. Lett.* **2004**, *85*, 2715–2717.

(53) Maissen, C.; Chen, S.; Nikulina, E.; Govyadinov, A.; Hillenbrand, R. Probes for ultra-sensitive THz nanoscopy. *ACS Photonics* **2019**, *6*, 1279–1288.

(54) Siday, T.; Hale, L. L.; Hermans, R. I.; Mitrofanov, O. Resonance-enhanced terahertz nanoscopy probes. *ACS Photonics* **2020**, *7*, 596–601.

(55) Mooshammer, F.; Plankl, M.; Siday, T.; Zizlsperger, M.; Sandner, F.; Vitalone, R.; Jing, R.; Huber, M. A.; Basov, D.; Huber, R. Quantitative terahertz emission nanoscopy with multiresonant near-field probes. *Opt. Lett.* **2021**, *46*, 3572–3575.

(56) Aghamiri, N. A.; Huth, F.; Huber, A. J.; Fali, A.; Hillenbrand, R.; Abate, Y. Hyper-spectral time-domain terahertz nano-imaging. *Opt. Express* **2019**, *27*, 24231–24242.

(57) Babicheva, V. E.; Gamage, S.; Stockman, M. I.; Abate, Y. Near-field edge fringes at sharp material boundaries. *Opt. Express* **2017**, *25*, 23935–23944.

(58) Cvitković, A.; Ocelić, N.; Hillenbrand, R. Analytical model for quantitative prediction of material contrasts in scattering-type near-field optical microscopy. *Opt. Express* **2007**, *15*, 8550–8565.

(59) Ocelić, N. Quantitative near-field phonon-polariton spectroscopy. Ph.D. thesis, Technische Universität München, 2007.

(60) Taubner, T.; Hillenbrand, R.; Keilmann, F. Performance of visible and mid-infrared scattering-type near-field optical microscopes. *J. Microsc.* **2003**, *210*, 311–314.

Supplementary Materials: Near-field Nanoscopy of Terahertz Polaritons with Quantitative Dielectric Mapping

Xiao Guo,[†] Xin He,^{‡,¶} Zach Degnan,[‡] Bogdan C. Donose,[†] Karl Bertling,[†] Arkady Fedorov,^{‡,¶} Aleksandar D. Rakic,^{*,†} and Peter Jacobson^{*,‡}

[†]*School of Information Technology and Electrical Engineering, The University of Queensland, Brisbane, QLD 4072, Australia*

[‡]*School of Mathematics and Physics, The University of Queensland, Brisbane, QLD 4072, Australia*

[¶]*ARC Centre of Excellence for Engineered Quantum Systems, Brisbane, QLD 4072, Australia*

E-mail: a.rakic@uq.edu.au; p.jacobson@uq.edu.au

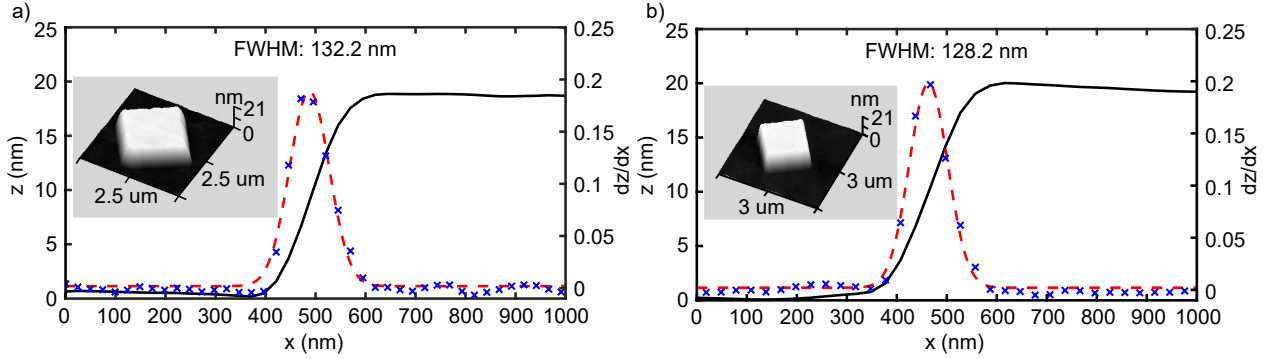


Figure S1: Line scan across a SiO_2 square (height variation: $20 \pm 1.5 \text{ nm}$) on Si substrate of commercial AFM calibration sample (TGQ1, TipsNano Co, Estonia) with different tips (25PtIr200B-H, Rocky Mountain Nanotechnology). Insets are the corresponding topography scans. The left axes show the scanning height (z) and the right axes show the spatial gradient of height (dz/dx). A Gaussian kernel is used for fitting to extract the corresponding full-width half maximum (FWHM) to obtain the information of tip radius and spatial resolution.

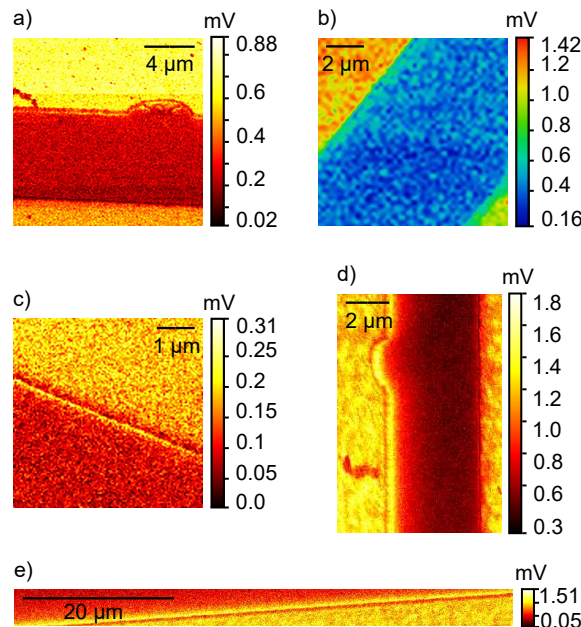


Figure S2: THz s-SNOM second-harmonic near-field scattering amplitudes for the chip processed before (a, b, c) and after etching (d, e) with various sample orientations. Within Fig. S2 (a, b, d), the area with higher scattering amplitude represents the area of the Al grounded plane, and the lowest signals are from Si channels. Fig. S2 (c) & (e) shows the field enhancement due to the edge effect that exists before (c) and after (e) etching.

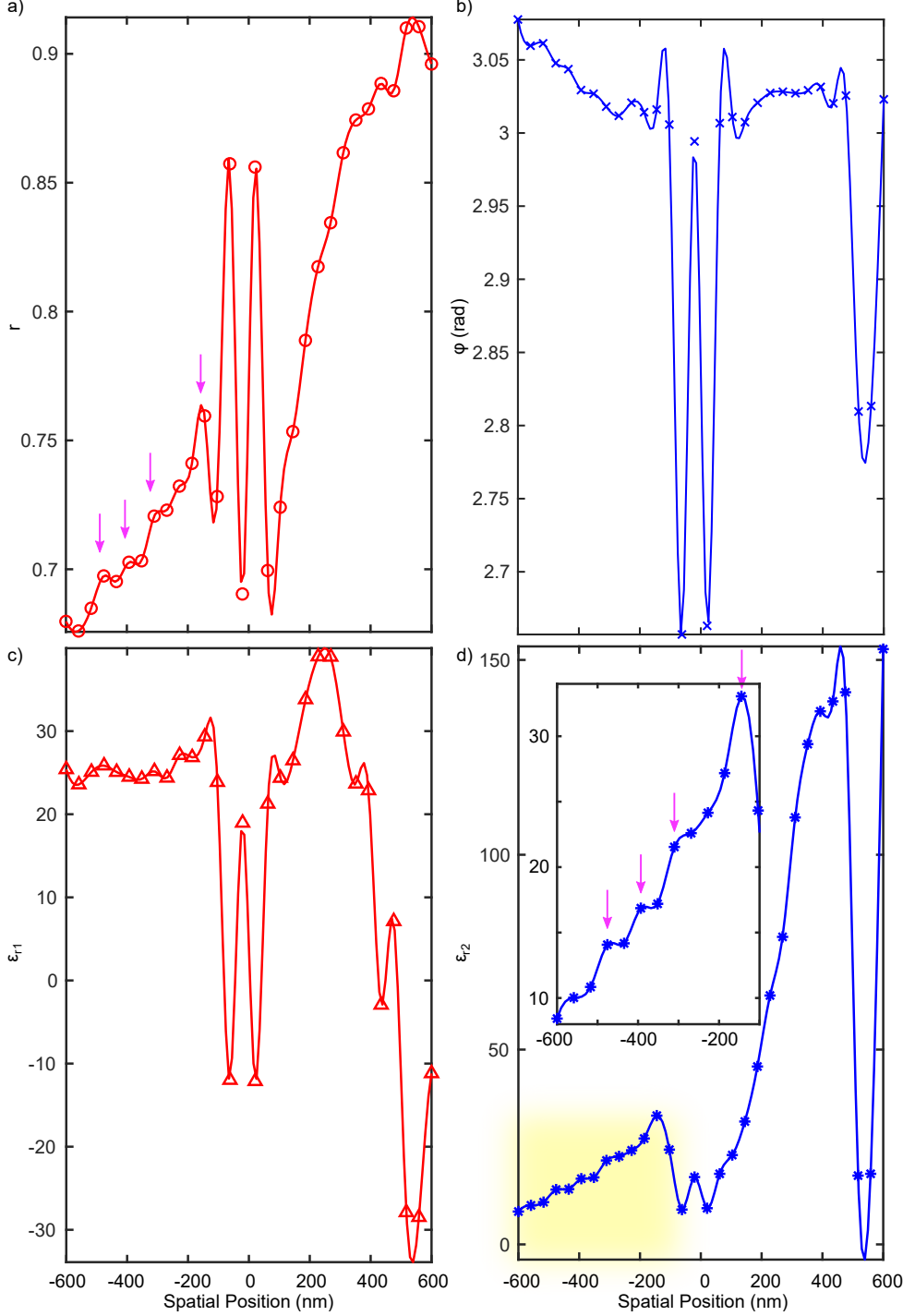


Figure S3: Extracted reflectivity (r), phase (ϕ), real (ϵ_{r1}) and imaginary (ϵ_{r2}) part of complex permittivity from THz hyperspectral scan at 0.85 THz. The representative fringes (denoted as the reflectivity fluctuation) superposed on an exponential decay field within the Si channel are highlighted with pink arrows in Fig. S3 (a). ϵ_{r2} response within the Si channel is highlighted by yellow shadow in Fig. S3 (d) and its inset shows the same fringe peaks characterized by ϵ_{r2} .

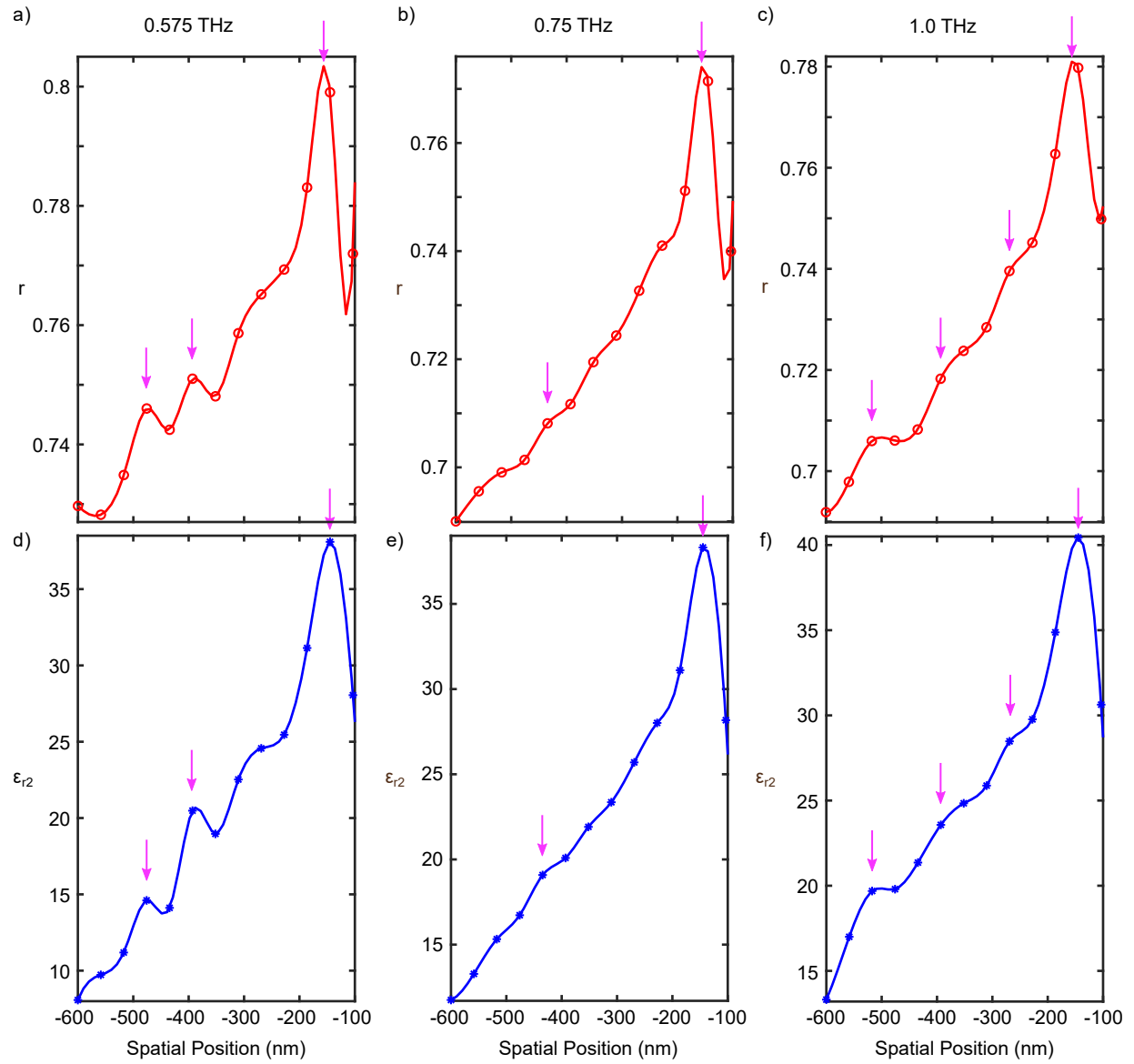


Figure S4: The spatial-varying relationship between r and ϵ_{r2} for localized fringe oscillations superposed on an exponential decay field within the Si channel at 0.575, 0.75 and 1.0 THz.